Journal of Computational Physics 438 (2021) 110360

Contents lists available at ScienceDirect

Journal of Computational Physics

www.elsevier.com/locate/jcp

A new finite element level set reinitialization method based on the shifted boundary method

Tianju Xue [a], WaiChing Sun [b], Sigrid Adriaenssens [a], Yujie Wei [c], Chuanqi Liu [c,*]

[a] Department of Civil and Environmental Engineering, Princeton University, Princeton, NJ 08544, USA
[b] Department of Civil Engineering and Engineering Mechanics, Columbia University, New York, NY, 10027, USA
[c] State Key Laboratory of Nonlinear Mechanics, Institute of Mechanics, Chinese Academy of Sciences, Beijing, 100090, China

ARTICLE INFO

Article history:
Available online 16 April 2021

Keywords:
Level set
Reinitialization
Shift boundary method

ABSTRACT

We propose an efficient method to reinitialize a level set function to a signed distance function by solving an elliptic problem using the finite element method. The original zero level set interface is preserved by means of applying modified boundary conditions to a surrogate/approximate interface weakly with a penalty method. Narrow band technique is adopted to reinforce the robustness of the proposed method where a smooth initial guess for the nonlinear equation is given by solving a Laplace's equation. Numerical benchmarks in both two dimensions and three dimensions confirm the optimal convergence rates under several different error measures including an interface error measure, showing that our method is accurate and robust. A three-dimensional genus 2 surface is adopted to demonstrate the capability of the method for the reinitialization of complicated geometries.

1. Introduction

1.1. The level set method and the signed distance function

The representation of an interface is of key importance for many numerical applications. These representations can be either implicit (via indicator function) or explicit (through node, edge and surface sets). In Lagrangian methods, a collection of points on the interface are identified such that the location of the interface in the spatial domain can be interpolated. Eulerian approaches employ a fixed mesh and represent the interface via a scalar-valued indicator function. The topological changes of the interfaces are thus handled by efficient Eulerian schemes. The level set method is based upon representing an interface as the zero level set of a scalar-valued function ϕ [1–4]. A signed distance function, which returns the Euclidean distance between a position to the closest interface, can be used as the indicator for interface. Suppose the interface Γ divides the total problem domain Ω into Ω^- and Ω^+, the signed distance function reads [5],

$$\phi(\boldsymbol{x}) = \begin{cases} -d & \text{for } \boldsymbol{x} \in \Omega^-, \\ +d & \text{for } \boldsymbol{x} \in \Omega^+, \\ 0 & \text{for } \boldsymbol{x} \in \Gamma, \end{cases} \tag{1}$$

* Corresponding author.
E-mail address: chuanqil@imech.ac.cn (C. Liu).

https://doi.org/10.1016/j.jcp.2021.110360
0021-9991/

where d is the Euclidian distance from $\boldsymbol{x}$ to Γ. Other choices exist for the construction of a level set function ϕ, but for stability purposes, it is often preferable to keep ϕ as a signed distance function [6]. Note that a signed distance function must satisfy the Eikonal equation,

$$|\nabla\phi| - 1 = 0, \tag{2}$$

where $\nabla(\cdot)$ denotes the spatial gradient operator and $|\cdot|$ is the Euclidean norm of a vector.

The level set interface $\phi(\boldsymbol{x}, t) = 0$ can be evolved through the solution of a scalar advection equation, e.g., the Hamilton-Jacobi equation. As the interface evolves, ϕ will generally drift away from its initialized value as a signed distance function, causing numerical instabilities [7]. Thus, central to the level set evolution problem is how to ensure that the level set function keeps close to a signed distance function throughout the time iterations. *Reinitialization* of the level set function to a signed distance function periodically during the evolution has been widely adopted as a numerical remedy for tackling this issue and maintaining stable curve evolution.

1.2. Methods to reinitialize level set

Among various reinitialization techniques, the hyperbolic reinitialization becomes particularly popular and has been extensively used [8–11]. The procedure is based on solving the following hyperbolic PDE (or its variants):

$$\frac{\partial\phi}{\partial\tau} + \text{sign}(\phi^0)(|\nabla\phi| - 1) = 0, \tag{3}$$

where $\frac{\partial\phi}{\partial\tau}$ is the pseudo temporal derivative of ϕ and ϕ^0 is the initial level set function to be reinitialized. The solution $\phi(\boldsymbol{x}, t)$ converges to the signed distance function as $\tau \to \infty$, which can be verified by solving the characteristic ordinary differential equation of (3). Among various types of finite difference solvers, the essentially nonoscillatory (ENO) method [12] with three-order accuracy and the weighted ENO (WENO) method [13,14] with fifth-order accuracy are most widely used for the spatial discretization. Min [15] compares the three temporal discretizations: the second-order Runge-Kutta method, the forward Euler method, and a Gauss-Seidel iteration of the forward Euler method and concludes that the Gauss-Seidel method is the best among the three. Unfortunately, if ϕ^0 is not smooth or ϕ^0 is much steeper on one side of the interface than the other, the zero level set interface of function ϕ can be moved incorrectly from that of ϕ^0 [16]. As pointed out in [17], the perturbations to the position of the original interface can lead to unpredictable results and the generation of fictitious elastic waves when using the level set to recapture the interface.

In contrast to the hyperbolic reinitialization approach, Basting and Kuzmin [18] propose to perform reinitialization by solving the following elliptic problem:

$$-\nabla\cdot\left(\nabla\phi - \frac{\nabla\phi}{|\nabla\phi|}\right) = 0. \tag{4}$$

The elliptic reinitialization methods do not require a temporal domain and thus have gained increased attentions in recent years [19–21]. While (4) appears to be easier to solve, it remains challenging to accurately impose the interface-preserving condition. To ensure that the interface is preserved, the zero level set interfaces of ϕ and ϕ^0 must be identical. As such, a Dirichlet boundary condition must be enforced at the location where $\phi^0 = 0$:

$$\phi = 0 \ \text{ on } \ \Gamma, \tag{5}$$

where Γ denotes the zero level set interface of ϕ^0.

Another class of methods enforce the Eiknoal equation constraint (2) implicitly either by imposing a penalty term [22] or a Lagrangian multiplier [23]. It should be mentioned that the fast marching method also can be used for reinitialization relying upwind finite differences. However, the original fast marching method cannot guarantee interfaces to be preserved. Chopp [24,25] modifies a Newton-Raphson iteration as a basis for the fast marching method. Rycroft [17] employs it to directly update the level set field, which maintains it as a signed distance function. Since we focus on the reinitialization problem, the numerical treatments for evolving interface are not considered here.

The proposed method falls into the category of elliptic reinitialization methods. With special treatment given to the imposition of condition (5), we introduce a simple, yet effective level set reinitialization technique inspired by the Shifted Boundary method, as reviewed in Section 1.3.

1.3. The Shifted Boundary method

The Shifted Boundary method is a method to represent complex geometries for embedded domain computations [26,27]. The key feature of the approach is to replace the constraints imposed on the true boundaries with constraints imposed on surrogate boundaries that are often composed by facets of finite element cells. The substitute constraints are derived from Taylor's series and only involve function values and their gradients on the surrogate boundaries. This method thus can

transfer the curved computation domain to a surrogate domain discretized with structured cells. This idea has been employed for shallow water flows [28], incompressible Navier-Stokes equations [29], Darcy flow problems [30], etc. Besides the finite element framework, it has also been extended and combined with other numerical frameworks, e.g., the imposition of Dirichlet boundary conditions for solid problems with the material point method [31].

1.4. Major objectives and overview of this article

The purpose of this paper is to introduce the Shifted Boundary concept to enable an interface-preserving reinitialization problem that does not require a temporal domain. As such, the zero level set interface in (5) is associated with the true interface Γ, whereas the surrogate interface is obtained from Taylor expansions. We thus propose a robust and easy-to-implement interface-preserving method for the reinitialization of level set functions. The paper is organized as follows. Section 2 introduces the method and some preliminaries. Section 3 presents a detailed discussion of the method, including practical improvements and adjustments on the basic version of the method. Section 4 shows several numerical examples in both 2D and 3D, with a particular focus on the convergence rates by several error measures. The paper closes with Section 5 as a conclusion.

2. Level set reinitialization with the Shifted Boundary method

2.1. Notations

Let $\Omega \subset \mathbb{R}^{n_d}$ (n_d is the number of space dimensions) be the problem domain with boundary $\partial\Omega$. Let $\mathcal{T}_h$ be a triangulation of Ω, consisting of non-overlapping elements Ω_e (squares for $n_d = 2$ or cubes for $n_d = 3$) such that $\Omega = \cup_{\Omega_e \in \mathcal{T}_h} \Omega_e$. We use h_e for the diameter of Ω_e and denote $h = \max_{\Omega_e \in \mathcal{T}_h} h_e$.

Let $W^{k,p}(\Omega)$ be the Sobolev space with norm

$$\|v\|_{W^{k,p}(\Omega)} = \begin{cases} \left(\sum_{|\alpha| \le k} \|\partial^\alpha v\|^p_{L^p(\Omega)} \right)^{1/p}, & 1 \le p < \infty, \\ \max_{|\alpha| \le k} \|\partial^\alpha v\|_{L^\infty(\Omega)}, & p = \infty, \end{cases} \tag{6}$$

where for multi-index α, $\partial^\alpha v$ is the α^{th} weak derivative of v. For $p = 2$, let $H^k(\Omega) = W^{k,2}(\Omega)$. By extension, the square-integrable function space $L^2(\Omega) = H^0(\Omega)$ and that $\|v\|_{L^2(\Omega)} = \|v\|_{H^0(\Omega)}$. Also, we have $\|v\|_{L^\infty(\Omega)} = \|v\|_{W^{0,\infty}(\Omega)}$.

2.2. The Shifted Boundary method preliminaries: the surrogate interface and the map

To illustrate the ideas of Shifted Boundary method, we consider a two-dimensional circle. As shown in Fig. 1, the blue circle with the boundary of Γ is embedded in a Eulerian domain Ω bounded by $\partial\Omega$. For each cell, we can determine whether the cell is inside, outside or cut by the boundary, according to the initial level set values at its vertices. If all nodal values for one cell are less than zero, the cell is inside the level set interface, and all inside cells collectively form a surrogate domain $\tilde{\Omega}$ with boundary of $\tilde{\Gamma}$, as shown in Fig. 1. We then construct a map $\boldsymbol{M}$ between the surrogate boundary $\tilde{\Gamma}$ to the level set interface Γ:

$$\boldsymbol{M} : \tilde{\Gamma} \to \Gamma, \tag{7a}$$

$$\tilde{\boldsymbol{x}} \mapsto \boldsymbol{x}, \tag{7b}$$

which maps a point $\tilde{\boldsymbol{x}} \in \tilde{\Gamma}$ on the surrogate interface, with outward-pointing unit normal denoted by $\tilde{\boldsymbol{n}}$, to a point $\boldsymbol{x} \in \Gamma$ on the level set interface with normal $\boldsymbol{n}$. For convenience, the map $\boldsymbol{M}$ can also be characterized by a distance vector function

$$\boldsymbol{d}(\tilde{\boldsymbol{x}}) = \boldsymbol{x} - \tilde{\boldsymbol{x}} = [\boldsymbol{M} - \boldsymbol{I}](\tilde{\boldsymbol{x}}), \tag{8}$$

which uses the closest-point projection for points in $\tilde{\Gamma}$ onto Γ, as shown in Fig. 1.

Suppose $\phi_D(\boldsymbol{x})$ is the boundary condition on Γ, and we want $\phi(\boldsymbol{x}) = \phi_D(\boldsymbol{x})$ on Γ. We can consider a Taylor expansion centered at $\tilde{\boldsymbol{x}} \in \tilde{\Gamma}$ for $\boldsymbol{x} = \boldsymbol{M}(\tilde{\boldsymbol{x}}) \in \Gamma$:

$$0 = \phi(\tilde{\boldsymbol{x}}) + \nabla\phi(\tilde{\boldsymbol{x}}) \cdot (\boldsymbol{x} - \tilde{\boldsymbol{x}}) - \phi_D(\boldsymbol{x}) + O\left(|\boldsymbol{x} - \tilde{\boldsymbol{x}}|^2\right) \tag{9a}$$

$$= \phi(\tilde{\boldsymbol{x}}) + \nabla\phi(\tilde{\boldsymbol{x}}) \cdot (\boldsymbol{M}(\tilde{\boldsymbol{x}}) - \tilde{\boldsymbol{x}}) - \phi_D(\boldsymbol{M}(\tilde{\boldsymbol{x}})) + O\left(|\boldsymbol{M}(\tilde{\boldsymbol{x}}) - \tilde{\boldsymbol{x}}|^2\right) \tag{9b}$$

$$= \phi(\tilde{\boldsymbol{x}}) + \nabla\phi(\tilde{\boldsymbol{x}}) \cdot \boldsymbol{d}(\tilde{\boldsymbol{x}}) - \phi_D(\boldsymbol{M}(\tilde{\boldsymbol{x}})) + O\left(|\boldsymbol{d}(\tilde{\boldsymbol{x}})|^2\right), \tag{9c}$$

where (9c) is readily on the surrogate interface $\tilde{\Gamma}$ to be imposed.

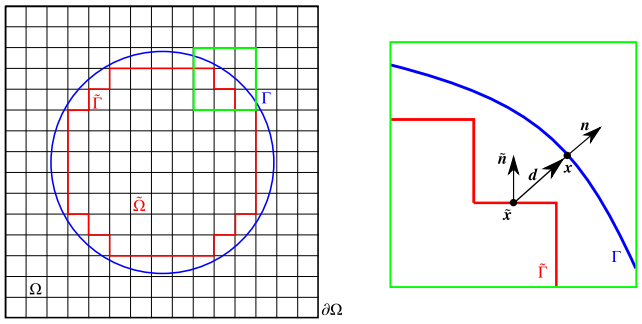

Fig. 1. Left: Problem domain Ω, its boundary $\partial\Omega$, the level set interface Γ, the surrogate interface $\tilde{\Gamma}$, and the embedded domain $\tilde{\Omega}$. Right: The map $\boldsymbol{M}$ characterized by the distance vector function $\boldsymbol{d}$, the point $\tilde{\boldsymbol{x}} \in \tilde{\Gamma}$, the mapped point $\boldsymbol{x} \in \Gamma$, the unit normal $\tilde{\boldsymbol{n}}$ with respect to $\tilde{\Gamma}$, and the unit normal $\boldsymbol{n}$ with respect to Γ. (For interpretation of the colors in the figure(s), the reader is referred to the web version of this article.)

Remark. For the signed distance function ϕ, we may obtain an extra benefit if the interface Γ is smooth. By nature of the signed distance function as shown in (1), the first order expansion of (9c) is actually exact and the following relationship holds for some $\tilde{\boldsymbol{x}} \in \Omega^-$ close to the interface Γ

$$\phi(\tilde{\boldsymbol{x}}) = -d = -\nabla\phi(\tilde{\boldsymbol{x}}) \cdot \boldsymbol{d}(\tilde{\boldsymbol{x}}), \tag{10}$$

where we have considered that ϕ must satisfy the Eikonal equation $|\nabla\phi| = 1$ and that $\nabla\phi(\tilde{\boldsymbol{x}})$ has the same direction as $\boldsymbol{d}(\tilde{\boldsymbol{x}})$. Compare (10) with (9c) while knowing $\phi_D = 0$, we realize that the residual $O\left(|\boldsymbol{d}(\tilde{\boldsymbol{x}})|^2\right)$ is zero. The term "smooth" is poorly defined here, but in the extreme case that Γ is a straight line, it is easy to verify that (10) is indeed satisfied, a beneficial property that other functions may not possess.

2.3. Elliptic level set reinitialization

First proposed by [22], the elliptic reinitialization strategy seeks to minimize a functional that measures how close the function ϕ is to a signed distance function,

$$\mathcal{P}(\phi) = \int_\Omega \frac{1}{2}(|\nabla\phi| - 1)^2 \, \mathrm{d}\Omega. \tag{11}$$

The functional $\mathcal{P}(\phi)$ essentially is the squares of residual to the Eikonal equation (2). The Euler-Lagrange equation associated with the functional (11) is computed as:

$$-\nabla \cdot \left(\nabla\phi - \frac{\nabla\phi}{|\nabla\phi|}\right) = 0 \ \text{ in } \ \Omega, \tag{12}$$

with a homogeneous Neumann boundary condition,

$$\left(\nabla\phi - \frac{\nabla\phi}{|\nabla\phi|}\right) \cdot \boldsymbol{t} = 0 \ \text{ on } \ \partial\Omega, \tag{13}$$

where $\boldsymbol{t}$ is the outward-pointing unit normal of $\partial\Omega$. To ensure that after reinitialization, the level set interface Γ is preserved, the following Dirichlet condition must be satisfied:

$$\phi = \phi_D \ \text{ on } \ \Gamma, \tag{14}$$

where $\phi_D = 0$ is set for this work. Combining (12), (13), and (14), we obtain the strong formulation of the elliptic reinitialization problem. (12) is a nonlinear Poisson equation such that a solution is obtained when $|\nabla\phi| = 1$.

Requiring less regularity, the weak formulation states that find $\phi \in H^1(\Omega)$ such that, $\forall \eta \in H^1(\Omega)$,

$$\int_\Omega \left(\nabla\phi - \frac{\nabla\phi}{|\nabla\phi|}\right) \cdot \nabla\eta \, \mathrm{d}\Omega + \mu \int_\Gamma (\phi - \phi_D)\eta \, \mathrm{d}\Gamma = 0, \tag{15}$$

where μ is a penalty parameter and the Dirichlet condition (14) is weakly imposed using a penalty term involving an integral on the level set interface Γ [18]. Also, the homogeneous Neumann boundary condition (13) is naturally satisfied in this formulation.

2.4. The proposed discretization

Note that (15) has three main features: (1) the volume integral is performed over the entire domain Ω; (2) the unknowns can be set at the nodes of a structured grid; and (3) the surface integral is along the true boundary, which is often unfitting to the edges of cells. It is apparently beneficial if we modify the third feature to an integral along the surrogate boundary (conformal to the edges of some cells) while keeping the other two features unchanged. The problem then reduces to how to transfer the constraint (14) imposed on Γ to $\tilde{\Gamma}$. Based on the Taylor expansion as shown in (9), we propose to use a new discretization strategy. Let $V^h(\Omega) \subset H^1(\Omega)$ be a discrete finite element subspace. The discretized weak formulation states that find $\phi_h \in V^h(\Omega)$ such that, $\forall \eta_h \in V^h(\Omega)$,

$$\boxed{\int_{\Omega} \left(\nabla \phi_h - \frac{\nabla \phi_h}{|\nabla \phi_h|} \right) \cdot \nabla \eta_h \, \mathrm{d}\Omega + \mu \int_{\tilde{\Gamma}} (\phi_h + \nabla \phi_h \cdot \boldsymbol{d} - \phi_D)(\eta_h + \nabla \eta_h \cdot \boldsymbol{d}) \, \mathrm{d}\tilde{\Gamma} = 0} \tag{16}$$

where $\boldsymbol{d}$ is the distance vector function introduced in (8). It is worth noting that (16) is different from the set up of the Shifted Boundary method originally proposed in [26,27], since the integral domain is the full domain containing the true interface, while it is a surrogate domain inside the true boundary in their work. However, note that a similar approach is used in [30] with the difference that we only have a primal variable ϕ to solve and there is no jump condition on the fluxes. The implementation of the method fits into the standard framework of the finite element methods, avoiding the need of any special treatment for the integral on Γ. The penalty parameter μ is set as

$$\mu = \frac{\alpha}{h_e}, \tag{17}$$

where α is a constant.

The weak form (16) is nonlinear. We use a Picard linearization to obtain simple and robust linear systems to solve for the reinitialization problem. Consequently, we obtain

$$a(\phi_h^{n+1}, \eta_h) = l(\phi_h^n, \eta_h), \tag{18}$$

where

$$a(\phi_h^{n+1}, \eta_h) = \int_{\Omega} \nabla \phi_h^{n+1} \cdot \nabla \eta_h \, \mathrm{d}\Omega + \mu \int_{\tilde{\Gamma}} (\phi_h^{n+1} + \nabla \phi_h^{n+1} \cdot \boldsymbol{d})(\eta_h + \nabla \eta_h \cdot \boldsymbol{d}) \, \mathrm{d}\tilde{\Gamma}, \tag{19a}$$

$$l(\phi_h^n, \eta_h) = \int_{\Omega} \frac{\nabla \phi_h^n \cdot \nabla \eta_h}{|\nabla \phi_h^n|} \, \mathrm{d}\Omega, \tag{19b}$$

in each Picard iteration. Here, ϕ_h^{n+1} is the unknown variable to solve in the current iteration and ϕ_h^n is known from the previous iteration.

It is straightforward to see that the bilinear form $a(\cdot, \cdot)$ of (19a) is symmetric. This form results in a symmetric linear system, practically easy to solve:

$$\boldsymbol{A}\boldsymbol{\phi} = \boldsymbol{l}, \tag{20}$$

where $\boldsymbol{\phi}$ is the vector of degrees of freedom, the system matrix $\boldsymbol{A} = (A_{ij})$ and the right hand side vector $\boldsymbol{l} = (l_i)$ are given by

$$A_{ij} = \int_{\Omega} \nabla \xi_j \cdot \nabla \xi_i \, \mathrm{d}\Omega + \mu \int_{\tilde{\Gamma}} (\xi_j + \nabla \xi_j \cdot \boldsymbol{d})(\xi_i + \nabla \xi_i \cdot \boldsymbol{d}) \, \mathrm{d}\tilde{\Gamma}, \tag{21a}$$

$$l_i = \int_{\Omega} \frac{\nabla \phi_h^n \cdot \nabla \xi_i}{|\nabla \phi_h^n|} \, \mathrm{d}\Omega, \tag{21b}$$

with ξ_i being the finite element basis function for the i^{th} degree of freedom.

3. Discussions on the proposed method

The goal of Section 2 is to present the essential elements constituting the proposed method for level set reinitialization in a concise and self-contained manner. However, various adjustments and improvements have been adopted for the method.

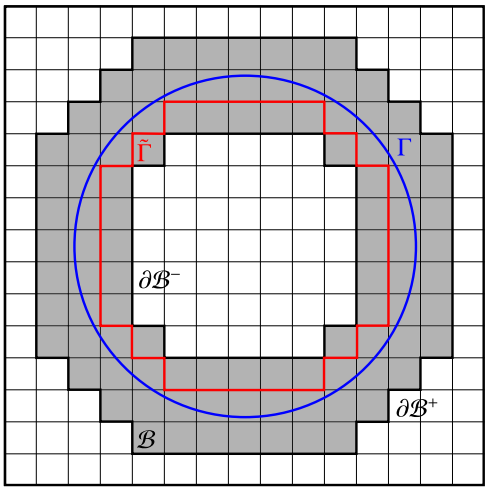

Fig. 2. The narrow band domain $\mathcal{B}$ for the gray area, its outer boundary $\partial\mathcal{B}^+$, and its inner boundary $\partial\mathcal{B}^-$.

Before we proceed to numerical tests in Section 4, we discuss several of these adjustments crucial for the efficiency of the proposed method in this section.

We will first introduce a popular technique called the narrow band approach which we adapt to significantly reduce the computational cost. Then we give a description on the two different maps associated with the Shifted Boundary method (see (7)) that we use for comparative studies in the subsequent numerical experiments. Finally, we point out an adjustment on the objective functional (11) to improve numerical stability of the reinitialization method.

3.1. The narrow band approach

When using the level set method, it is beneficial to adopt a narrow band approach [32] that solves the problem only in a thin band around the level set surface. The obvious advantage of this approach is to cut the computational cost down, e.g., from $O(N^2)$ to $O(kN)$ in two dimensions, where N is the number of degrees of freedom in each space dimension and k is the width of the narrow band.

Reducing computational cost is not the only benefit of the narrow band level set method. When the level set surface encloses a simply-connected region (e.g., a circle), there will always be a singularity for the signed distance function (e.g., the center of the circle). Numerical methods tend to be sensitive to the smoothness of the exact solution. The existence of singularity may deteriorate the order of convergence for a method designed to be of higher order, as studied in [21]. When the computation of the signed distance function is restricted to a narrow band domain that excludes the singularity point, the problem no longer exists.

In this work, the narrow band domain $\mathcal{B}$ is determined using a heuristic approach. We first identify all the elements that are cut by the interface Γ, which already forms a narrow band. Being conservative, we iteratively expand the narrow band by adding more elements into the set of the current narrow band collection of elements. In each iteration, those elements sharing a common face with any elements in the collection will be marked as to add to the collection after the iteration. A narrow band domain after one such iteration is illustrated in Fig. 2, with the outer boundary denoted by $\partial\mathcal{B}^+$ and the inner boundary denoted by $\partial\mathcal{B}^-$.

One caveat that is often times overlooked is that if the initial level set function ϕ^0 is significantly different from a signed distance function, the reinitialization schemes may not be able to reinitialize the function to a signed distance function [23]. In the context of elliptic level set reinitialization methods, our numerical experiments have also corroborated this statement. A third benefit of using a narrow band approach coupled with our reinitialization method now emerges: we propose to mitigate this issue by using a smooth function ψ in $\mathcal{B}$ as to replace ϕ^0 for the initial guess of Picard iteration (18). To construct ψ as a close approximation of the signed distance function, we can solve a Laplace's equation in $\mathcal{B}$. The strong form of the problem states that find $\psi \in C^2(\Omega)$ such that,

$$-\Delta\psi = 0 \ \text{ in } \ \mathcal{B}, \tag{22a}$$

$$\psi = k/2 \ \text{ on } \ \partial\mathcal{B}^+, \tag{22b}$$

$$\psi = -k/2 \ \text{ on } \ \partial\mathcal{B}^-, \tag{22c}$$

where k is the band width. Note that the map $\boldsymbol{M}$ is always constructed based on ϕ^0, but other than that, ϕ^0 can be safely replaced by ψ as a good initial start. This proposed trick is practically useful and makes our reinitialization method more independent of the quality of ϕ^0. However, in the full domain Ω, it is not immediately clear how such ψ can be constructed.

3.2. Considerations for maps

It follows that when using the closest-point projection method to build $\boldsymbol{M}$ for a certain point $\tilde{\boldsymbol{x}} \in \tilde{\Gamma}$, we essentially require

$$\phi^0(\boldsymbol{x}) = 0, \tag{23a}$$

$$\boldsymbol{d}(\boldsymbol{x}) \times \boldsymbol{n}(\boldsymbol{x}) = \boldsymbol{0}, \tag{23b}$$

as illustrated in Fig. 1, where condition (23a) is equivalent to $\boldsymbol{x} \in \Gamma$ and condition (23b) fulfills closest-point projection. We can rewrite condition (23b) as

$$(\boldsymbol{x} - \tilde{\boldsymbol{x}}) \times \nabla\phi^0(\boldsymbol{x}) = \boldsymbol{0}. \tag{24}$$

To solve for $\boldsymbol{x}$, we adopt an iterative procedure based on a two-step Newton's method [24]:

$$\boldsymbol{\delta}_1 = -\phi^0(\boldsymbol{x}^n)\frac{\nabla\phi^0(\boldsymbol{x}^n)}{\nabla\phi^0(\boldsymbol{x}^n)\cdot\nabla\phi^0(\boldsymbol{x}^n)}, \tag{25a}$$

$$\boldsymbol{x}^{n+1/2} = \boldsymbol{x}^n + \boldsymbol{\delta}_1, \tag{25b}$$

$$\boldsymbol{\delta}_2 = (\tilde{\boldsymbol{x}} - \boldsymbol{x}^n) - \frac{(\tilde{\boldsymbol{x}} - \boldsymbol{x}^n)\cdot\nabla\phi^0(\boldsymbol{x}^n)}{\nabla\phi^0(\boldsymbol{x}^n)\cdot\nabla\phi^0(\boldsymbol{x}^n)}\nabla\phi^0(\boldsymbol{x}^n), \tag{25c}$$

$$\boldsymbol{x}^{n+1} = \boldsymbol{x}^{n+1/2} + \boldsymbol{\delta}_2. \tag{25d}$$

The procedure alternately updates $\boldsymbol{x}$ so that the two conditions in (23) are approximately satisfied. The convergence criterion is set when $\sqrt{|\boldsymbol{\delta}_1|^2 + |\boldsymbol{\delta}_2|^2} < \epsilon$, with $\epsilon > 0$ being a small threshold.

3.3. Objective functionals

The proposed reinitialization method is based on the minimization of the least squares residual to the Eikonal equation, as presented in (11) that be rewritten as

$$\mathcal{P}_1(\phi) = \int_\Omega t_1(|\nabla\phi|)\,\mathrm{d}\Omega, \tag{26}$$

where

$$t_1(|\nabla\phi|) = \frac{1}{2}(|\nabla\phi| - 1)^2. \tag{27}$$

Correspondingly, the strong form (12) is rewritten as

$$-\nabla\cdot(d_1(|\nabla\phi|)\nabla\phi) = 0 \ \text{ in } \ \Omega, \tag{28}$$

where

$$d_1(|\nabla\phi|) = 1 - \frac{1}{|\nabla\phi|}. \tag{29}$$

This formulation is natural at its appearance, but it has several intrinsic drawbacks. For instance, the diffusion term d_1 becomes singular as $|\nabla\phi| \to 0$, leading to numerical difficulties. To overcome the issues, an alternative formulation is proposed by [18]:

$$t_2(|\nabla\phi|) = \begin{cases} \frac{1}{2}(|\nabla\phi| - 1)^2 & \text{if } |\nabla\phi| > 1, \\ \frac{1}{2}|\nabla\phi|^2(|\nabla\phi| - 1)^2 & \text{if } |\nabla\phi| \le 1, \end{cases} \tag{30}$$

along with

$$d_2(|\nabla\phi|) = \begin{cases} 1 - \dfrac{1}{|\nabla\phi|} & \text{if } |\nabla\phi| > 1, \\ 1 - (3|\nabla\phi| - 2|\nabla\phi|^2) & \text{if } |\nabla\phi| \le 1. \end{cases} \tag{31}$$

The formulation introduces new issues in that the functional defined by t_2 has multiple extrema. As extensively discussed by [21], a third formulation is proposed as

$$t_3(|\nabla\phi|) = \begin{cases} \frac{1}{2}(|\nabla\phi| - 1)^2 & \text{if } |\nabla\phi| > 1, \\ \frac{1}{3}|\nabla\phi|^3 - \frac{1}{2}|\nabla\phi|^2 + \frac{1}{6} & \text{if } |\nabla\phi| \leq 1, \end{cases} \tag{32}$$

along with

$$d_3(|\nabla\phi|) = \begin{cases} 1 - \dfrac{1}{|\nabla\phi|} & \text{if } |\nabla\phi| > 1, \\ 1 - (2 - |\nabla\phi|) & \text{if } |\nabla\phi| \leq 1. \end{cases} \tag{33}$$

In this work, we adopt t_3 and d_3 in all our numerical examples. Under this modification, we introduce minor revisions to the original formulation and adjust (16) to be

$$\int_\Omega \left(\nabla\phi_h - \Big(1 - d_3(|\nabla\phi_h|)\Big)\nabla\phi_h\right) \cdot \nabla\eta_h \, \mathrm{d}\Omega + \mu \int_{\tilde{\Gamma}} (\phi_h + \nabla\phi_h \cdot \boldsymbol{d} - \phi_D)(\eta_h + \nabla\eta_h \cdot \boldsymbol{d}) \, \mathrm{d}\tilde{\Gamma} = 0. \tag{34}$$

The rest formulation from (18) to (21) should also be modified accordingly, whose details we omit.

4. Numerical results

4.1. Error measures

When an analytical solution ϕ exists, we can measure the errors in the L^2, H^1, L^∞ and L^1 norms, i.e.,

$$\mathcal{E}_{L^2} = \|\phi_h - \phi\|_{L^2(\Omega)}, \tag{35}$$

$$\mathcal{E}_{H^1} = \|\phi_h - \phi\|_{H^1(\Omega)}, \tag{36}$$

$$\mathcal{E}_{L^\infty} = \|\phi_h - \phi\|_{L^\infty(\Omega)}, \tag{37}$$

and

$$\mathcal{E}_{L^1} = \|\phi_h - \phi\|_{L^1(\Omega)}. \tag{38}$$

When the analytical solution is not known, we can introduce two additional metrics to measure errors [21]. The first one measures the degree to which the Eikonal equation (2) is satisfied, i.e.,

$$\mathcal{E}_{\mathrm{SD}} = \left(\int_\Omega (|\nabla\phi_h| - 1)^2 \, \mathrm{d}\Omega\right)^{1/2}, \tag{39}$$

which will be referred to as the *signed distance error measure*. The second one is a measure of the movement of the level set interface Γ in the L^2 sense. We compute the surface integral of the square values of the approximate solution along Γ:

$$\mathcal{E}_{\mathrm{Int}} = \left(\int_\Gamma \phi_h^2 \, \mathrm{d}\Gamma\right)^{1/2}, \tag{40}$$

which will be referred to as the *interface error measure*.

We further introduce the *volume error measure* defined as

$$\mathcal{E}_{\mathrm{Vol}} = \left|\frac{V - V_0}{V_0}\right|, \tag{41}$$

where V is the volume of the interior domain defined by ϕ_h, and V_0 is the volume before reinitialization defined by ϕ^0.

When computing $\mathcal{E}_{L^2}$, $\mathcal{E}_{H^1}$ $\mathcal{E}_{L^\infty}$, $\mathcal{E}_{L^1}$, and $\mathcal{E}_{\mathrm{SD}}$, we always integrate over the narrow band domain for fair comparison, i.e., always set $\Omega = \mathcal{B}$ even if the computation itself is in the full domain. It is shown in [26] that the optimal convergence for a linear Poisson problem with Shifted Boundary method remains to be h^2 in the L^2 norm and h^1 in the H^1 norm. For the nonlinear Poisson problem discussed in this work, we expect a similar performance for the order of convergence. Besides, the signed distance error $\mathcal{E}_{\mathrm{SD}}$ evaluates the difference between measures of the gradient of the solution, so we expect the order of convergence to be similar as if measured in the H^1 norm. Reference lines are added in these scenarios for better comparisons with the results.

The following statements are true for all subsequent numerical experiments. The domain Ω is set to be $\Omega = [-2, 2]^{n_d}$. We stop the Picard iteration of (18) if $|\boldsymbol{\phi}^{n+1} - \boldsymbol{\phi}^n| < 10^{-8}$ or the number of iterations exceeds 1000. A penalty constant $\alpha = 10$ is used in (17). We perform $h-$convergence studies for several numerical examples. A sequence of uniform Cartesian meshes with square elements of size $h = 0.176, 0.088, 0.044, 0.022$ are used for $n_d = 2$ and meshes with cubic elements of size $h = 0.216, 0.108, 0.054$ for $n_d = 3$. When constructing narrow band domains, a band width $k = 9$ is used for $n_d = 2$ and $k = 3$ for $n_d = 3$. The reported order of convergence (OC) is computed using the difference between the coarsest mesh and the finest mesh. First order continuous Galerkin finite element is used throughout the tests. The code is developed based on the `deal.II` finite element library [33,34].

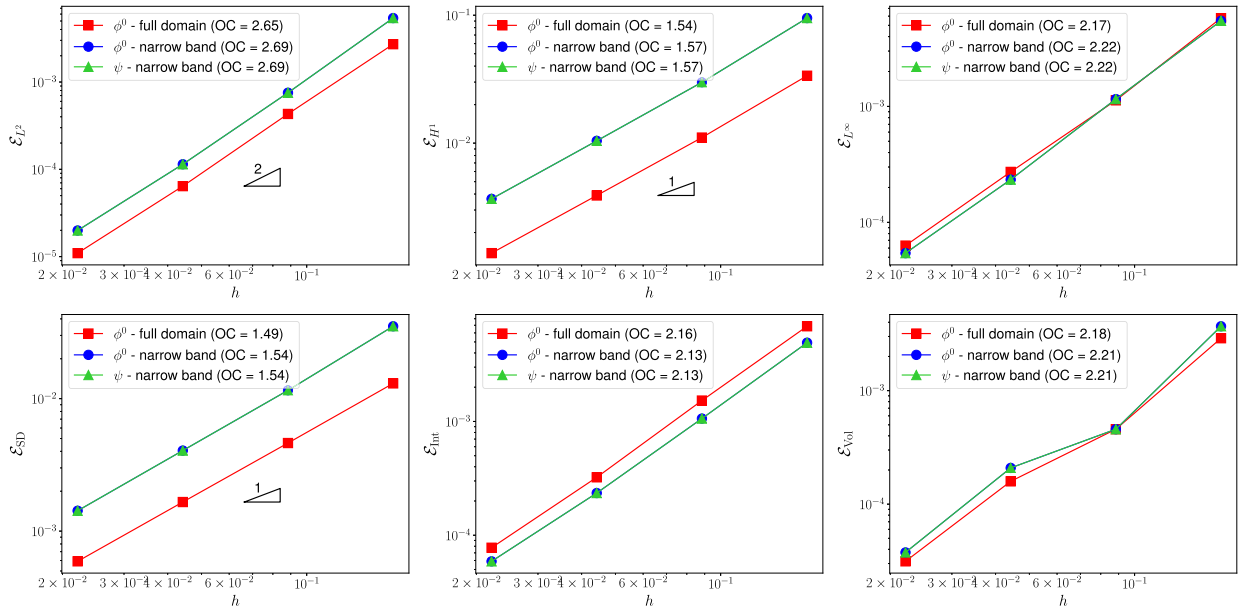

Fig. 3. Error measures $\mathcal{E}_{L^2}$, $\mathcal{E}_{H^1}$, $\mathcal{E}_{L^\infty}$, $\mathcal{E}_{\mathrm{SD}}$, $\mathcal{E}_{\mathrm{Int}}$, and $\mathcal{E}_{\mathrm{Vol}}$, and convergence rates for the circular interface problem. The legend ϕ^0 – full domain means that we use ϕ^0 as the initial guess and solve the problem in the full domain. Similar for the others.

4.2. Circular interface

The first test case contains a circular interface initially described by the level set function ϕ^0 such that

$$\phi^0 = x^2 + y^2 - 1. \tag{42}$$

The exact signed distance function can be represented as

$$\phi = \sqrt{x^2 + y^2} - 1. \tag{43}$$

Since analytical solutions exist, we use $\mathcal{E}_{L^2}$, $\mathcal{E}_{H^1}$, $\mathcal{E}_{L^\infty}$, $\mathcal{E}_{\mathrm{SD}}$, $\mathcal{E}_{\mathrm{Int}}$, and $\mathcal{E}_{\mathrm{Vol}}$ as the error estimates and report the results in Fig. 3. We first conduct the numerical experiments in the full domain $\Omega = [-2, 2] \times [-2, 2]$ with ϕ^0 as the initial guess. We then run the simulations with a narrow band strategy with the initial guess being ϕ^0 or a smooth function ψ obtained by solving the Laplace's equation (22). Results show that the use of ψ produces nearly the same error measures compared with ϕ^0. Since errors are computed in the narrow band domain that excludes singular point, we obtain optimal convergence in terms of $\mathcal{E}_{L^2}$, $\mathcal{E}_{H^1}$, and $\mathcal{E}_{\mathrm{SD}}$. Furthermore, the successful use of ψ releases us from a high demand on the quality of the initial level set function ϕ^0.

4.3. Interface with four-fold symmetry

For numerical tests with more complex geometries, we propose to construct an interface with four-fold symmetry by considering the following initial level set function [35]

$$\phi^0 = r^2 - \big(1 - 0.2\cos(4\theta) + 0.2\cos(8\theta)\big), \tag{44}$$

where $r \geq 0$ and $\theta \in [0, 2\pi)$ are polar coordinates:

$$x = r\cos(\theta), \tag{45a}$$

$$y = r\sin(\theta). \tag{45b}$$

An illustration of the interface shape is shown in Fig. 4.

The initial level set function (44) deviates from the signed distance function and an analytical solution is not known. We therefore use $\mathcal{E}_{\mathrm{SD}}$ and $\mathcal{E}_{\mathrm{Int}}$ as the error measures. The volume of the interior is known to be π, so we can also compute $\mathcal{E}_{\mathrm{Vol}}$. Fig. 5 shows the convergence of errors in both the full domain and the narrow band domain. Optimal convergence rates are obtained in $\mathcal{E}_{\mathrm{SD}}$. We can also confirm the discussions in the previous circular interface case about the different choices for initial guesses.

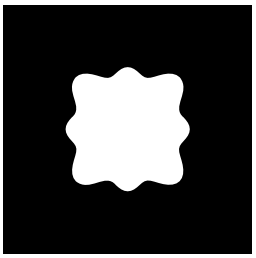

Fig. 4. Interface with four-fold symmetry obtained from (44). For the white area we have $\phi^0 < 0$ while for the black area we have $\phi^0 > 0$.

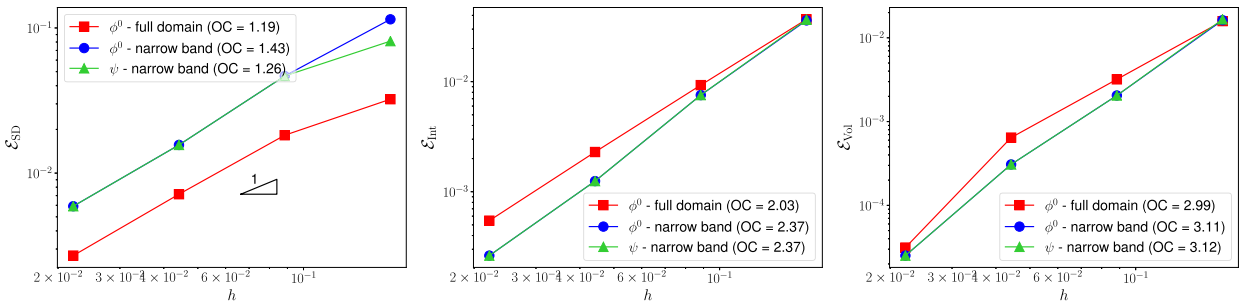

Fig. 5. Error measures $\mathcal{E}_{\mathrm{SD}}$, $\mathcal{E}_{\mathrm{Int}}$, and $\mathcal{E}_{\mathrm{Vol}}$ and convergence rates for the four-fold symmetric interface problem. The legend ϕ^0 – full domain means that we use ϕ^0 as the initial guess and solve the problem in the full domain. Similar for the others.

When computing $\mathcal{E}_{\mathrm{Int}}$, an integral over the implicit surface Γ is involved. An accurate estimate of this integral in the unfitted background mesh is nontrivial in general. However, the particular parametric form of the interface of (44) allows to use a simple quadrature method, hence suppressing any error associated with the methods for integration over Γ. For completeness, we show the numerical integration for an arbitrary function $f(x, y)$ on Γ as

$$\int_{\Gamma} f(x, y)\, \mathrm{d}\Gamma = \int_{[0,2\pi]} \hat{f}(\theta, \phi)\sqrt{r(\theta)^2 + r'(\theta)^2}\, \mathrm{d}\theta, \tag{46}$$

where $\hat{f}(\theta) = f(x(r(\theta), \theta), y(r(\theta), \theta))$, $r(\theta) = \sqrt{1 + c_1 \cos(4\theta) + c_2 \cos(8\theta)}$ by (44), and $\mathrm{d}\Gamma = \sqrt{r(\theta)^2 + r'(\theta)^2}\, \mathrm{d}\theta$ is the arc length transformation to polar coordinates. A conservative number of 100,000 quadrature points are used to evaluate $\mathcal{E}_{\mathrm{Int}}$ following the trapezoidal rule, ensuring that the error associated with performing numerical integration has minimal effect on our convergence reports.

4.4. Interface with kinks

To show the capacity of the proposed method for the case with kinks, we consider a 2D interface formed by two intersected circles both with radius r and located at $(\pm a, 0)$, as used in [15]. The exact signed distance function can be written as

$$\phi = \begin{cases} \min\left(\sqrt{x^2 + \left(y \pm \sqrt{r^2 - a^2}\right)^2}\right) & \text{if } \dfrac{a - x}{\sqrt{(a-x)^2 + y^2}} \geq \dfrac{a}{r} \text{ and } \dfrac{a + x}{\sqrt{(a+x)^2 + y^2}} \geq \dfrac{a}{r}, \\ \min\left(\sqrt{(x \pm a)^2 + y^2} - r\right) & \text{else}, \end{cases} \tag{47}$$

where we take $r = 1$ and $a = 0.7$. The signed distance function ϕ has kinks on a line segment $[-a, a]$ along the x-axis as well as on intervals $(-\infty, -\sqrt{r^2 - a^2}]$ and $[\sqrt{r^2 - a^2}, \infty)$ along the y-axis. As a result, gradient of the signed distance function $\nabla\phi$ is not well defined on these line segments. It should be reminded that $\nabla\phi$ is only required at quadrature points either inside the surrogate domain or on the surrogate boundary (see formulation (16)), which is typically available in practice.

For the initial level set function, we first set $\phi^{0,a}$ as used in [15] to compare the proposed method and the reinitialization schemes with their finite difference methods such that

$$\phi^{0,a} = \phi \cdot \left[(x-1)^2 + (y-1)^2 + 0.1\right]. \tag{48}$$

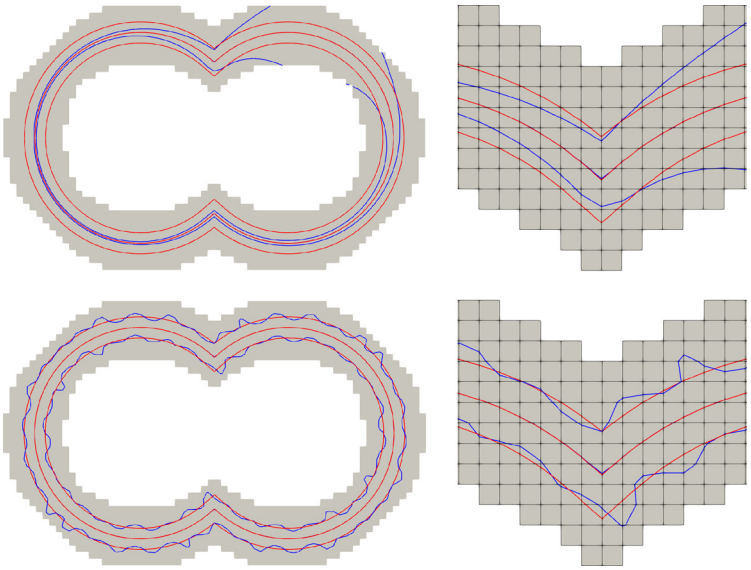

Fig. 6. Contour plots of the level set function before/after reinitialization using the method of this work with a narrow band approach ($h = 0.088$). The upper two figures show the contours of $\phi^{0,a} = -0.1, 0, 0.1$ (blue) and $\phi = -0.1, 0, 0.1$ (red), where the upper right subfigure is a local magnification for the kink with grid on. The lower two figures show the contours of $\phi^{0,b} = -0.1, 0, 0.1$ (blue) and $\phi = -0.1, 0, 0.1$ (red), where the lower right subfigure is a local magnification for the kink with grid on.

We then test the robustness of the proposed method with a second choice of the initial level set functions $\phi^{0,b}$ containing oscillatory terms as

$$\phi^{0,b} = \phi \cdot [0.5\sin(6\pi x)\sin(6\pi y) + 1]. \tag{49}$$

Fig. 6 illustrates the contours of the level set functions before/after reinitialization for both $\phi^{0,a}$ and $\phi^{0,b}$ using the proposed method. We can see that the interface is well preserved after reinitialization, even near the kink region.

To compare the accuracy, we implement classic reinitialization methods based on solving a hyperbolic PDE (see equation (3)) by the finite difference method. As a baseline, the original scheme proposed in [8] is employed with forward Euler for temporal discretization and second order ENO finite difference for spatial discretization. An improved version [15] with a subcell fix technique to preserve the interface is also adopted. Maintaining all other conditions the same, we perform reinitialization for both $\phi^{0,a}$ and $\phi^{0,b}$ with standard finite difference approach [8], improved finite difference method with subcell fix [15], and finite element method of this work, respectively. We report the error measures $\mathcal{E}_{L^1}$ and $\mathcal{E}_{\text{Int}}$ in Fig. 7. As shown, in all cases finite difference reinitialization method with subcell fix and finite element reinitialization method of this work achieve lower error compared with the baseline method. For both $\phi^{0,a}$ and $\phi^{0,b}$, our method yields lower interface error compared with the subcell fix approach, while the errors are similar in the L^1 norm. These results show that our method is competitive in terms of accuracy, especially for preserving the interface location and holding a relatively low interface error.

To compare the efficiency, although the reinitialization method with subcell fix scheme is effective, this is the result of fine tuning the time step parameter so that the method can converge relatively quickly (e.g., see Fig. 8 for the time evolution). In contrast, our method avoids the temporal domain, and is free from dealing with difficulties arising from time discretization. The proposed method is therefore efficient in its simplicity.

4.5. Spherical interface

A spherical interface in 3D is initially described by the level set function ϕ^0 such that

$$\phi^0 = x^2 + y^2 + z^2 - 1. \tag{50}$$

The exact signed distance function can be represented as

$$\phi = \sqrt{x^2 + y^2 + z^2} - 1. \tag{51}$$

It should be noted that the proposed reinitialization method generalizes from 2D to 3D trivially. When implementing the scheme in `deal.II`, we only need to provide a different number for the dimensional argument in the function template and the library allows for dimension-independent programming for the rest of the code.

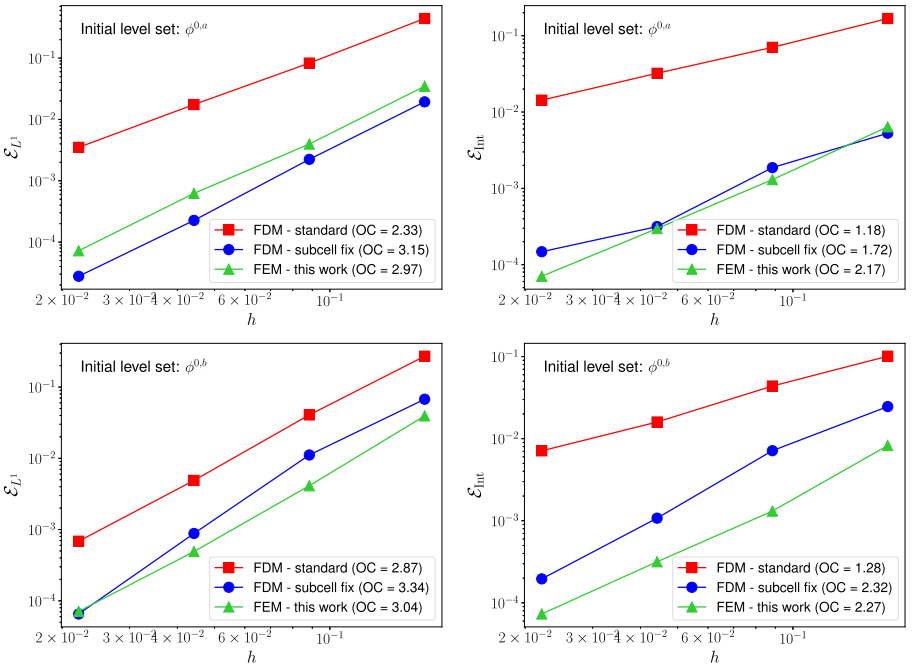

Fig. 7. Error measures $\mathcal{E}_{L^1}$ and $\mathcal{E}_{\text{Int}}$ and convergence rates for the baseline finite difference reinitialization method (red), the finite difference reinitialization method with subcell fix (blue), and the finite element reinitialization method of this work (green). The upper two figures use $\phi^{0,a}$ as the initial level set function, while the lower two figures use $\phi^{0,b}$. All results are computed with narrow band domains.

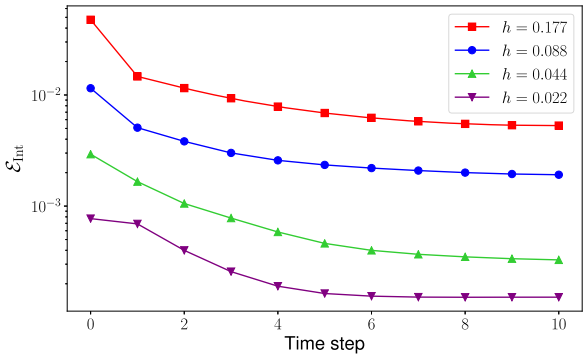

Fig. 8. Convergence in $\mathcal{E}_{\text{Int}}$ for the finite difference reinitialization method with subcell fix using $\phi^{0,a}$ as the initial level set function.

In Fig. 9, we show the cross-sectional views of the solution ϕ_h ($h = 0.054$) with a local magnification for the narrow band region. For clarification, we still use a uniform mesh for the narrow band domain $\mathcal{B}$. The "adaptive mesh refinement" shown in Fig. 9 actually reflects a strategy we use to determine the narrow band region. In `Deal.II`, one may be tempted to start with a globally refined mesh and then search for the narrow band. We point out that this naive approach can be significantly expensive since the connectivity of a full mesh has to be stored, though the actual finite element computation should only appear in the narrow band region. Therefore we propose to use an adaptive strategy to search for the narrow band region. In summary, the strategy starts with a relatively coarse mesh, searches for a narrow band region containing Γ, and then only refines the cells in that region. Repeatedly, we restrict ourselves to the refined region, identify a narrow band and perform refinement. Fig. 9 shows the result of performing two such cycles.

As shown in Fig. 10, a complete set of error measures $\mathcal{E}_{L^2}$, $\mathcal{E}_{H^1}$, $\mathcal{E}_{L^\infty}$, $\mathcal{E}_{\text{SD}}$, $\mathcal{E}_{\text{Int}}$, and $\mathcal{E}_{\text{Vol}}$ are available. We observe optimal rates of convergence for $\mathcal{E}_{L^2}$, $\mathcal{E}_{H^1}$, and $\mathcal{E}_{\text{SD}}$, similarly as in 2D examples. In particular, the order of convergence for $\mathcal{E}_{H^1} = 1.52$ is close to $\mathcal{E}_{\text{SD}} = 1.50$ as expected.

To evaluate $\mathcal{E}_{\text{Int}}$, we need to be able to compute integrals on Γ. For an arbitrary function $f(x, y, z)$ on a spherical surface, it is straightforward to see that

$$\int_{\Gamma} f(x, y, z)\, \mathrm{d}\Gamma = \int_{[0,2\pi]\times[0,\pi]} \hat{f}(\beta, \gamma) a^2 \sin(\beta)\, \mathrm{d}\beta\, \mathrm{d}\gamma, \tag{52}$$

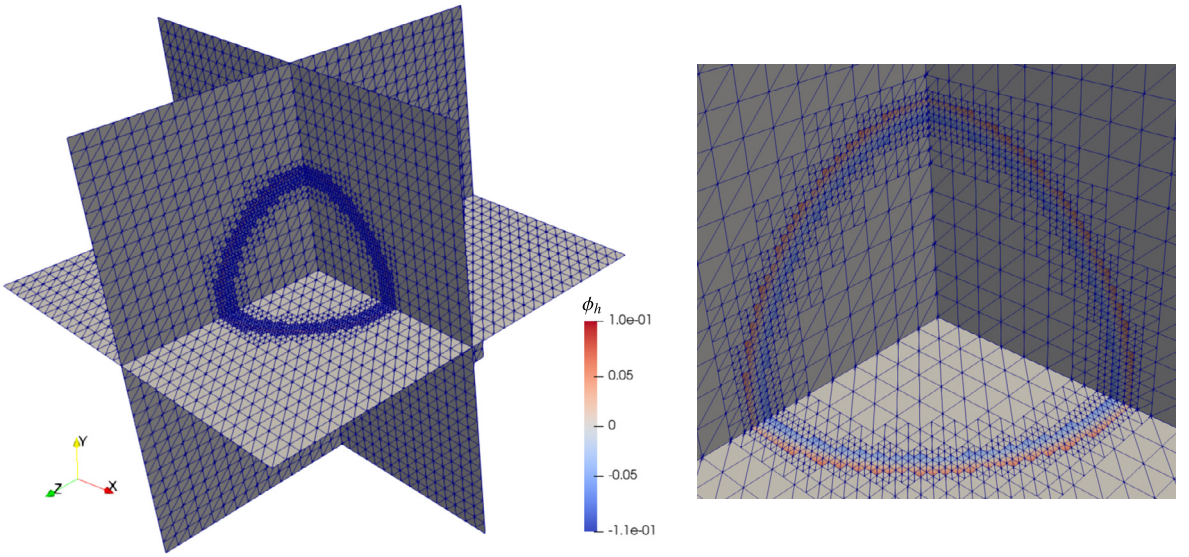

Fig. 9. Demonstrations of a spherical surface. Left: orthogonal cross-sectional views of the solution ϕ_h. Right: a local magnification for the narrow band region. The "adaptive mesh refinement" is only a reflection of the strategy adopted to determine the narrow band region. The actual finite element computation is still performed in a uniform mesh.

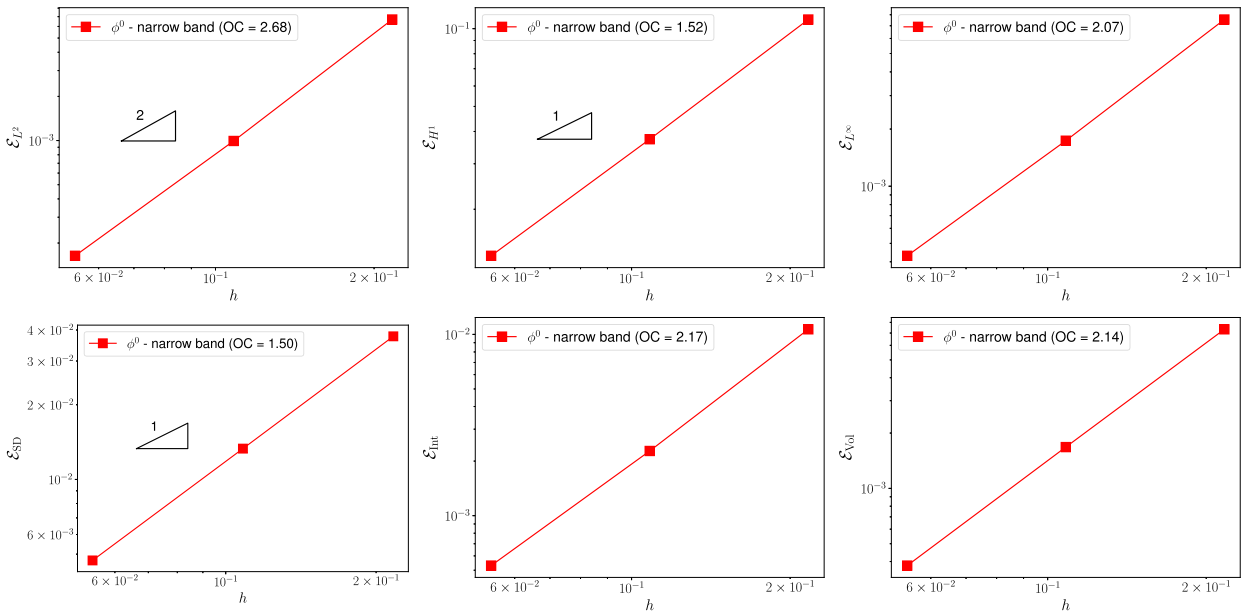

Fig. 10. Error measures $\mathcal{E}_{L^2}$, $\mathcal{E}_{H^1}$, $\mathcal{E}_{L^\infty}$, $\mathcal{E}_{\mathrm{SD}}$, $\mathcal{E}_{\mathrm{Int}}$, and $\mathcal{E}_{\mathrm{Vol}}$, and convergence rates for the circular interface problem. Results are computed using ϕ^0 as the initial guess and solving the problem in the narrow band domain.

where $\hat{f}(\beta,\gamma) = f(x,y,z)$, the radius $a = 1$, and $\mathrm{d}\Gamma = a^2\sin(\beta)\,\mathrm{d}\beta\,\mathrm{d}\gamma$ is the area transformation to spherical coordinates with

$$x = a\sin(\beta)\cos(\gamma), \tag{53a}$$

$$y = a\sin(\beta)\sin(\gamma), \tag{53b}$$

$$z = a\cos(\beta). \tag{53c}$$

A relatively large number of $2,000 \times 1,000 = 2,000,000$ quadrature points are used to evaluate $\mathcal{E}_{\mathrm{Int}}$, ensuring that the error associated with performing numerical integration has minimal affect.

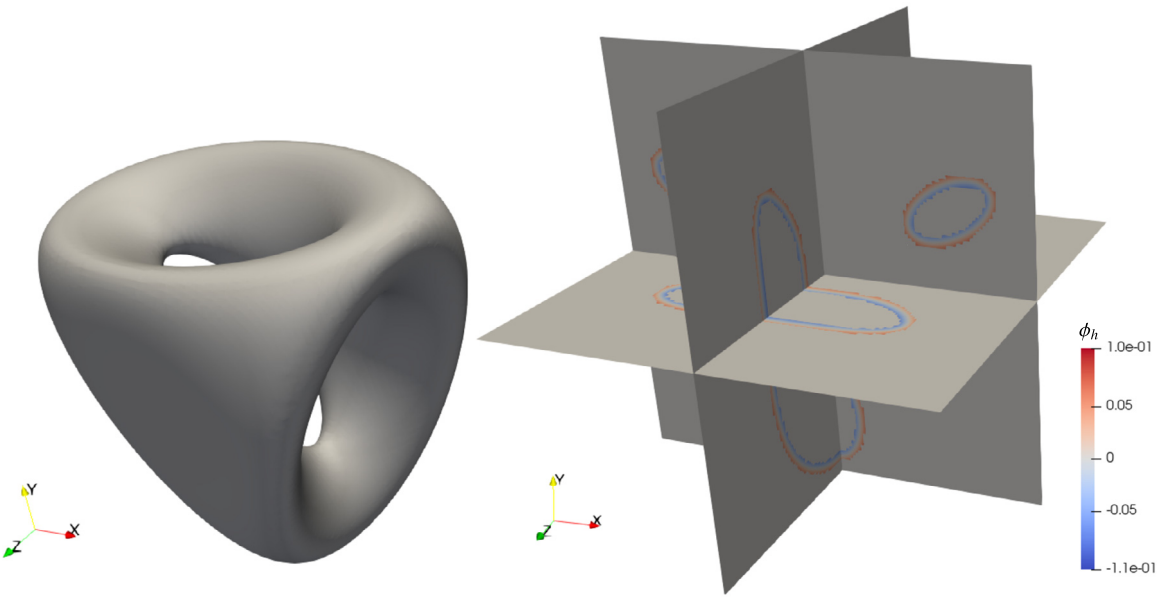

Fig. 11. Demonstrations of a genus 2 surface. Left: the zero level set interface $\phi^0 = 0$ by (54). Right: orthogonal cross-sectional views of the solution ϕ_h in the narrow band region with mesh turned off.

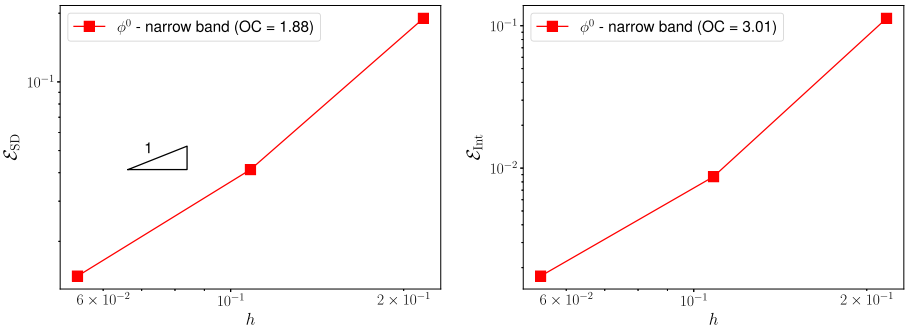

Fig. 12. Error measures $\mathcal{E}_{SD}$ and $\mathcal{E}_{Int}$, and convergence rates for the genus 2 interface problem. Results are computed using ϕ^0 as the initial guess and solving the problem in the narrow band domain.

4.6. Genus 2 interface

In topology, the genus of a surface, is the number of "holes" it has, so that a sphere has genus 0 and a torus has genus 1 [36]. As a test bed, we consider the initial level set function ϕ^0 whose zero contour defines the surface of a genus 2:

$$\phi^0 = 2y(y^2 - 3x^2)(1 - z^2) + (x^2 + y^2)^2 - (9z^2 - 1)(1 - z^2), \tag{54}$$

where the analytical solution for the signed distance function is not known.

As an illustration, Fig. 11 shows the zero level set interface $\phi^0 = 0$ by (54) and the cross-sectional views of the solution ϕ_h ($h = 0.054$) in the narrow band region.

We use $\mathcal{E}_{SD}$ and $\mathcal{E}_{Int}$ as the error measures and show the results in Fig. 12. For this complex surface in 3D, we are also able to obtain the optimal convergence rates, showing that our reinitialization method is reliable.

In this final example, the accurate evaluation of $\mathcal{E}_{Int}$ poses a challenge since the implicit surface defined by (54) may not have a simple parametric representation, hence the integral over Γ becomes nontrivial. We propose, for the first time, the Shifted Interface Integration Method (SIIM) to resolve this issue. We consider SIIM as an efficient, accurate, and generic numerical integration method for an implicitly defined interface. Since the method is rather independent of the main body of this work, we leave the description of the method and its full justification in Appendix A. The interface error measure $\mathcal{E}_{Int}$ in Fig. 12 is evaluated by SIIM.

5. Conclusions

In this paper, we have proposed a robust and easy-to-implement method for level set reinitialization that leverages the Shifted Boundary method to simplify the numerical procedures. The governing equation for the signed distance function fits into the class of elliptic reinitialization techniques and hence does not require the introduction of an artificial temporal domain. The boundary condition, i.e., $\phi = 0$, imposed on the true boundary is weakly imposed onto a surrogate boundary $\tilde{\Gamma}$ which is composed of edges of structured cells. The map between the true boundary and the surrogate boundary is constructed by closest point projection using the initial level set field to ensure interface preserving. The proposed method is reinforced by the narrow band technique and a smooth guess for the nonlinear equation is also given to enhance the robustness of the method. The benchmarks show that the proposed method can preserve the interface and the errors follow h^2 in the L^2 norm and h^1 in the H^1 norm. A three-dimensional genus 2 surface is adopted to show the capability of the method for the reinitialization of complicated geometries. The future work will focus on initializing level sets and constructing signed distance functions from various input formats, such as binary images.

CRediT authorship contribution statement

Tianju Xue: Investigation, software, original draft preparation. Waiching Sun: Methodology. Sigrid Adriaenssens: Reviewing and Editing. Yujie Wei: Reviewing and Editing. Chuanqi Liu: Conceptualization, Supervision.

Declaration of competing interest

The authors declare that they have no known competing financial interests or personal relationships that could have appeared to influence the work reported in this paper.

Acknowledgments

Yujie Wei and Chuanqi Liu are supported by the National Key Research and Development Program of China (2017YFB0202800) and the One Hundred Talents Program (Pioneering Project) of Chinese Academy of Sciences (CAS). Tianju Xue and Sigrid Adriaenssens gratefully acknowledge the financial support of the Princeton Catalysis Initiative (Princeton University). WaiChing Sun's involvement is supported by the National Science Foundation, United States of America grant from the Mechanics of Materials and Structures program under grant contracts CMMI-1846875 and the Office of Advanced Cyberinfrastructure under grant contracts OAC-1940203.

Appendix A. The Shifted Interface Integration Method (SIIM)

Numerical integration on an implicitly defined interface is a common problem in many disciplines. In the setup of an unfitted background mesh, several successful strategies include subdivision based methods [37,38], Monte-Carlo techniques [39], and moment fitting methods [40]. Despite their achievements, these methods may not be the most suited for our work due to certain limitations. Methods based on subdivision of the background mesh typically rely on a re-meshing procedure and create additional sub-elements conformal to the interface. This class of methods are easy to perceive but remain a hassle for implementation and fundamentally disagree with the unfitted nature of the background mesh. Monte-Carlo methods suffer from being computationally prohibitive due to an excessive number of evaluations required to achieve a satisfactory accuracy. The moment-fitting method proposed by [40] also has certain limitations. The method requires to solve a potentially ill-conditioned linear system to determine the quadrature weights of each cut cell, based on a set of divergence-free basis functions that are subjective to construct.

In the context of the Shifted Boundary method, we propose a simple, yet efficient and robust method to perform numerical integration on an implicit surface Γ defined by a level set function. We call the method Shifted Interface Integration Method (SIIM). In short, the method transforms the intractable integral on the interface Γ to a tractable integral on the shifted interface $\tilde{\Gamma}$, with the closest-point projection map $\boldsymbol{M}$ being the bridge. As noted in [26], the map $\boldsymbol{M}$ is actually smooth given certain regularity of Γ.

Let us consider the integral $\mathcal{I}$ of a given function $f(\boldsymbol{x})$ on Γ

$$\mathcal{I} = \int_{\Gamma} f(\boldsymbol{x}) \, \mathrm{d}\Gamma = \int_{\tilde{\Gamma}} \tilde{f}(\tilde{\boldsymbol{x}}) \frac{\mathrm{d}\Gamma}{\mathrm{d}\tilde{\Gamma}}(\tilde{\boldsymbol{x}}) \, \mathrm{d}\tilde{\Gamma} \approx \sum_q \tilde{f}(\tilde{\boldsymbol{x}}_q) \tilde{j}(\tilde{\boldsymbol{x}}_q) \tilde{w}_q = \sum_q f(\boldsymbol{x}_q) w_q, \tag{A.1}$$

where $\tilde{f}(\tilde{\boldsymbol{x}}) = f(\boldsymbol{M}(\tilde{x}))$, $(\tilde{\boldsymbol{x}}_q, \tilde{w}_q)$ are the q^{th} quadrature point and weight on $\tilde{\Gamma}$, $(\boldsymbol{x}_q, w_q)$ are the q^{th} quadrature point and weight on Γ, $\tilde{j}(\tilde{\boldsymbol{x}}) = \frac{\mathrm{d}\Gamma}{\mathrm{d}\tilde{\Gamma}}(\tilde{\boldsymbol{x}})$ represents the arc length ratio (2D) or surface area ratio (3D) for the differentials. The quadrature points and weights $(\tilde{\boldsymbol{x}}_q, \tilde{w}_q)$ are standard on the surrogate interface $\tilde{\Gamma}$. It is also straightforward to evaluate $\tilde{f}(\tilde{\boldsymbol{x}}_q)$ and the only thing left is the evaluation of $\tilde{j}(\tilde{\boldsymbol{x}}_q)$.

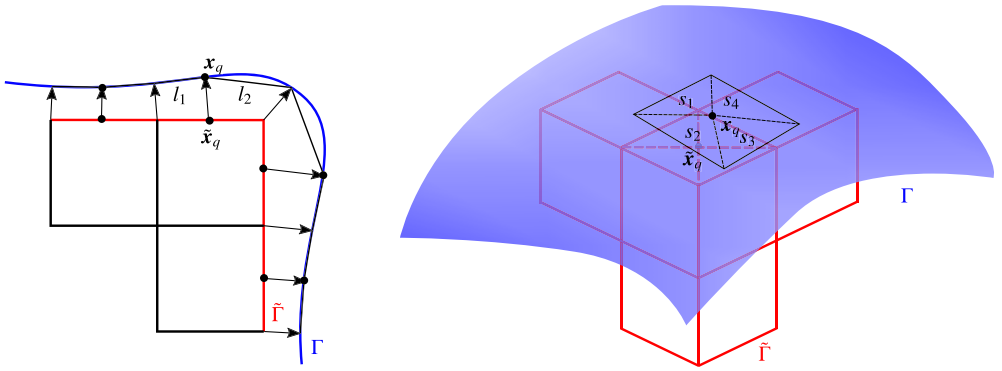

Fig. 13. Demonstrations of SIIM. The left and right figures correspond to 2D and 3D situations, respectively. A single quadrature point $\tilde{\boldsymbol{x}}_q$ on each element face is used in the illustration, with the corresponding quadrature point $\boldsymbol{x}_q$ on Γ. In the 2D case, l_1 and l_2 denote the lengths of the two line segments. In the 3D case, s_1, s_2, s_3 and s_4 denote the areas of the four triangles.

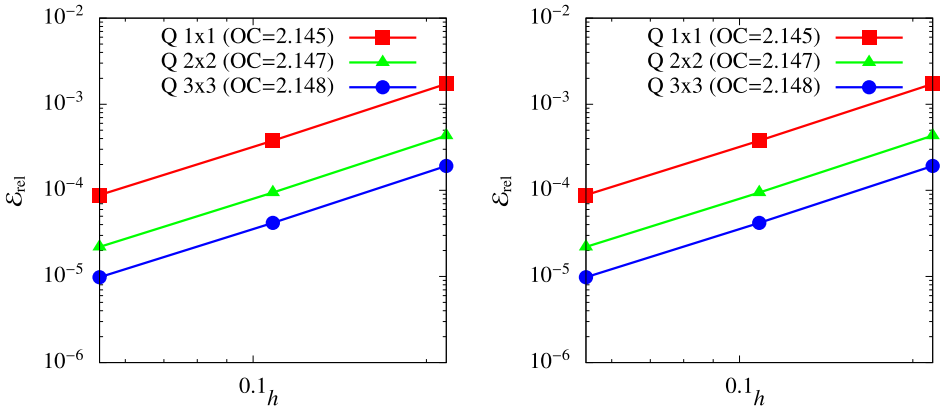

Fig. 14. Relative errors $\mathcal{E}_{\text{rel}}$ and convergence rates for the integrals in (A.3). The left figure shows integral (A.3a) and the right figure shows integral (A.3b) The legend "Q 3x3" means to use $3 \times 3 = 9$ quadrature points per element face, similar meanings for "Q 2x2" and "Q 1x1".

For simplicity, we assume a single quadrature point is used at each element face. As shown in Fig. 13, we approximate $\tilde{j}(\tilde{\boldsymbol{x}}_q)$ by

$$\tilde{j}(\tilde{\boldsymbol{x}}_q) \approx \frac{l_1 + l_2}{l} \quad \text{in 2D}, \tag{A.2a}$$

$$\tilde{j}(\tilde{\boldsymbol{x}}_q) \approx \frac{s_1 + s_2 + s_3 + s_4}{s} \quad \text{in 3D}, \tag{A.2b}$$

where l is the element face length in 2D and s is the element face area in 3D. The presented strategy generalizes naturally for more quadrature points.

Another view of SIIM is through the last equation in the chain of (A.1). It is equivalent to perceive the method as performing quadrature integration directly on Γ with an automatic subdivision of the true interface Γ, in light of the map $\boldsymbol{M}$.

To justify the accuracy of SIIM, we consider a spherical interface defined in (42). We use SIIM to compute numerical integration on the following integrals:

$$\int_\Gamma \mathrm{d}\Gamma = 4\pi\,, \tag{A.3a}$$

$$\int_\Gamma (4 - 3x^2 + 2y^2 - z^2)\,\mathrm{d}\Gamma = \frac{40}{3}\pi\,. \tag{A.3b}$$

As shown in Fig. 14, the two integrals report similar results for different number of quadrature points used. The convergence rates are stable for all the scenarios.

To further demonstrate that SIIM produces reliable results for the evaluation of the interface error measure $\mathcal{E}_{\text{Int}}$, we show a comparison between SIIM and the parametric integration method by (52) for evaluating $\mathcal{E}_{\text{Int}}$ in Section 4.5. The later is

Table 1
A comparison between SIIM (using $3 \times 3 = 9$ quadrature points per element face) and the parametric integration method by (52) for evaluating $\mathcal{E}_{\text{Int}}$ in the spherical interface case.

h	0.216	0.108	0.054
SIMM (Q 3x3)	1.06671×10^{-2}	2.27435×10^{-3}	5.30345×10^{-4}
Parametric integration method by (52)	1.06686×10^{-2}	2.27603×10^{-3}	5.32535×10^{-4}

used to report $\mathcal{E}_{\text{Int}}$ in Fig. 10. In Table 1, we show that the interface error measures $\mathcal{E}_{\text{Int}}$ are close for both SIMM and the parametric method. Viewing the parametric method as the ground truth, we can safely consider SIMM to be accurate for the error estimation.

In short, we have proposed a general integration method for an interface implicitly defined by a level set function. The method is easy to perceive and simple to implement, while still being accurate and robust. Independent of the main body of this paper, SIIM can be a potential contribution to techniques of numerical integration.

References

[1] J.A. Sethian, Level Set Methods and Fast Marching Methods: Evolving Interfaces in Computational Geometry Fluid Mechanics, Computer Vision, and Materials Science, vol. 3, Cambridge University Press, 1999.
[2] S. Osher, R. Fedkiw, K. Piechor, Level set methods and dynamic implicit surfaces, Appl. Mech. Rev. 57 (2004), B15.
[3] J. Huang, H. Zhang, Level set method for numerical simulation of a cavitation bubble, its growth, collapse and rebound near a rigid wall, Acta Mech. Sin. 23 (2007) 645–653.
[4] S. Phongthanapanich, P. Dechaumphai, An explicit finite volume element method for solving characteristic level set equation on triangular grids, Acta Mech. Sin. 27 (2011) 911–921.
[5] F. Gibou, R. Fedkiw, S. Osher, A review of level-set methods and some recent applications, J. Comput. Phys. 353 (2018) 82–109.
[6] W. Mulder, S. Osher, J.A. Sethian, Computing interface motion in compressible gas dynamics, J. Comput. Phys. 100 (1992) 209–228.
[7] D.L. Chopp, Computing minimal surfaces via level set curvature flow, 1991.
[8] M. Sussman, P. Smereka, S. Osher, A level set approach for computing solutions to incompressible two-phase flow, J. Comput. Phys. 114 (1994) 146–159.
[9] D. Peng, B. Merriman, S. Osher, H. Zhao, M. Kang, A pde-based fast local level set method, J. Comput. Phys. 155 (1999) 410–438.
[10] M. Sussman, E. Fatemi, An efficient, interface-preserving level set redistancing algorithm and its application to interfacial incompressible fluid flow, SIAM J. Sci. Comput. 20 (1999) 1165–1191.
[11] J. Zhang, P. Yue, A high-order and interface-preserving discontinuous Galerkin method for level-set reinitialization, J. Comput. Phys. 378 (2019) 634–664.
[12] A. Harten, B. Engquist, S. Osher, S.R. Chakravarthy, Uniformly high order accurate essentially non-oscillatory schemes, iii, in: Upwind and High-Resolution Schemes, Springer, 1987, pp. 218–290.
[13] X.-D. Liu, S. Osher, T. Chan, et al., Weighted essentially non-oscillatory schemes, J. Comput. Phys. 115 (1994) 200–212.
[14] G.-S. Jiang, C.-W. Shu, Efficient implementation of weighted eno schemes, J. Comput. Phys. 126 (1996) 202–228.
[15] C. Min, On reinitializing level set functions, J. Comput. Phys. 229 (2010) 2764–2772.
[16] S. Osher, R.P. Fedkiw, Level Set Methods and Dynamic Implicit Surfaces, vol. 1, Springer, New York, 2005.
[17] C.H. Rycroft, F. Gibou, Simulations of a stretching bar using a plasticity model from the shear transformation zone theory, J. Comput. Phys. 231 (2012) 2155–2179.
[18] C. Basting, D. Kuzmin, A minimization-based finite element formulation for interface-preserving level set reinitialization, Computing 95 (2013) 13–25.
[19] A. Caboussat, R. Glowinski, T.-W. Pan, On the numerical solution of some Eikonal equations: an elliptic solver approach, Chin. Ann. Math., Ser. B 36 (2015) 689–702.
[20] A.G. Belyaev, P.-A. Fayolle, On Variational and Pde-Based Distance Function Approximations, Computer Graphics Forum, vol. 34, Wiley Online Library, 2015, pp. 104–118.
[21] T. Adams, S. Giani, W.M. Coombs, A high-order elliptic pde based level set reinitialisation method using a discontinuous Galerkin discretisation, J. Comput. Phys. 379 (2019) 373–391.
[22] C. Li, C. Xu, C. Gui, M.D. Fox, Level set evolution without re-initialization: a new variational formulation, in: 2005 IEEE Computer Society Conference on Computer Vision and Pattern Recognition (CVPR'05), vol. 1, IEEE, 2005, pp. 430–436.
[23] M.K. Touré, A. Soulaïmani, Stabilized finite element methods for solving the level set equation without reinitialization, Comput. Math. Appl. 71 (2016) 1602–1623.
[24] D.L. Chopp, Some improvements of the fast marching method, SIAM J. Sci. Comput. 23 (2001) 230–244.
[25] D.L. Chopp, Another look at velocity extensions in the level set method, SIAM J. Sci. Comput. 31 (2009) 3255–3273.
[26] A. Main, G. Scovazzi, The shifted boundary method for embedded domain computations. Part i: Poisson and Stokes problems, J. Comput. Phys. 372 (2018) 972–995.
[27] A. Main, G. Scovazzi, The shifted boundary method for embedded domain computations. Part ii: linear advection–diffusion and incompressible Navier–Stokes equations, J. Comput. Phys. 372 (2018) 996–1026.
[28] T. Song, A. Main, G. Scovazzi, M. Ricchiuto, The shifted boundary method for hyperbolic systems: embedded domain computations of linear waves and shallow water flows, J. Comput. Phys. 369 (2018) 45–79.
[29] E.N. Karatzas, G. Stabile, L. Nouveau, G. Scovazzi, G. Rozza, A reduced-order shifted boundary method for parametrized incompressible Navier–Stokes equations, Comput. Methods Appl. Mech. Eng. 370 (2020) 113273.
[30] K. Li, N.M. Atallah, G.A. Main, G. Scovazzi, The shifted interface method: a flexible approach to embedded interface computations, Int. J. Numer. Methods Eng. 121 (2020) 492–518.
[31] C. Liu, W. Sun, Shift boundary material point method: an image-to-simulation workflow for solids of complex geometries undergoing large deformation, Comput. Part. Mech. 7 (2020) 291–308.
[32] D. Adalsteinsson, J.A. Sethian, A fast level set method for propagating interfaces, J. Comput. Phys. 118 (1995) 269–277.
[33] D. Arndt, W. Bangerth, B. Blais, T.C. Clevenger, M. Fehling, A.V. Grayver, T. Heister, L. Heltai, M. Kronbichler, M. Maier, P. Munch, J.-P. Pelteret, R. Rastak, I. Thomas, B. Turcksin, Z. Wang, D. Wells, The deal.II library, version 9.2, J. Numer. Math. 28 (2020) 131–146.
[34] D. Arndt, W. Bangerth, D. Davydov, T. Heister, L. Heltai, M. Kronbichler, M. Maier, J.-P. Pelteret, B. Turcksin, D. Wells, The deal.II finite element library: design, features, and insights, Comput. Math. Appl. (2020).

[35] T. Xue, A. Beatson, M. Chiaramonte, G. Roeder, J.T. Ash, Y. Menguc, S. Adriaenssens, R.P. Adams, S. Mao, A data-driven computational scheme for the nonlinear mechanical properties of cellular mechanical metamaterials under large deformation, Soft Matter 16 (2020) 7524–7534.
[36] J.R. Munkres, Topology, 2000.
[37] C. Min, F. Gibou, Geometric integration over irregular domains with application to level-set methods, J. Comput. Phys. 226 (2007) 1432–1443.
[38] D.J. Holdych, D.R. Noble, R.B. Secor, Quadrature rules for triangular and tetrahedral elements with generalized functions, Int. J. Numer. Methods Eng. 73 (2008) 1310–1327.
[39] Y.-S. Liu, J. Yi, H. Zhang, G.-Q. Zheng, J.-C. Paul, Surface area estimation of digitized 3d objects using quasi-Monte Carlo methods, Pattern Recognit. 43 (2010) 3900–3909.
[40] B. Müller, F. Kummer, M. Oberlack, Highly accurate surface and volume integration on implicit domains by means of moment-fitting, Int. J. Numer. Methods Eng. 96 (2013) 512–528.